2. J. Deisenhofer and H. Michel, *Science* **245**, 1463 (1989).
3. R. M. Baum, *Chem. Eng. News* (22 February 1993), p. 20.
4. C. C. Moser, J. M. Keske, K. Warncke, R. S. Farid, P. L. Dutton, *Nature* **355**, 796 (1992).
5. D. N. Beratan, J. N. Betts, J. N. Onuchic, *Science* **252**, 1285 (1991); J. N. Onuchic, D. N. Beratan, J. R. Winkler, H. B. Gray, *Annu. Rev. Biophys. Biomol. Struct.* **21**, 349 (1992) and references therein.
6. J. W. Evenson and M. Karplus, *J. Chem. Phys.* **96**, 5272 (1992).
7. D. N. Beratan, J. N. Betts, J. N. Onuchic, *J. Phys. Chem.* **96**, 2852 (1992).
8. R. A. Marcus and N. Sutin, *Biochim. Biophys. Acta* **811**, 265 (1985); *J. Chem. Phys.* **24**, 966 (1956); *Discuss. Faraday Soc.* **29**, 21 (1960); *J. Chem. Phys.* **43**, 679 (1965); N. S. Hush, *ibid.* **28**, 964 (1958); *Trans. Faraday Soc.* **57**, 557 (1961).
9. M. D. Newton, *Chem. Rev.* **91**, 767 (1991).
10. E. N. Economou, *Green's Functions in Quantum Physics* (Springer-Verlag, Berlin, 1990).
11. J. W. Evenson and M. Karplus, unpublished results.
12. The correlation coefficient of two random variables X and Y is (*23*)
$$\rho(x,y) = \frac{E(XY) - E(X)E(Y)}{\sigma_x \sigma_y} \qquad (4)$$
where $E(Z)$ is the expectation value of the random variable Z, and σ_z^2 is its variance. The correlation coefficient is bounded: $|\rho(X,Y)| \leq 1$. The equality holds if and only if Y depends linearly on X. Indeed, $Y = mX + b$ implies $\rho(X,Y) = m/|m|$, so that the sign of ρ agrees with the sign of the slope. If X and Y are uncorrelated, $\rho(X,Y) = 0$.
13. H. M. McConnell, *J. Chem. Phys.* **35**, 508 (1961).
14. In (*6*), we showed that the effective coupling for the 1D model decays monotonically for $|\alpha| > 1$ and exponentially only for $|\alpha| >> 1$. The subtle distinction between rapid monotonic decay and pure exponential decay is revealed in the present formalism by values of the correlation coefficient that approach, but never exactly equal, −1. The 1D results imply that as $|\alpha|$ becomes large, the correlation coefficient becomes arbitrarily close to −1, and this is confirmed by our calculations for cytochrome c. We call all behavior with $|\alpha| > 1$ exponential because in applications, it appears essentially exponential.
15. Coordinates were obtained from the file pdb5cyt.ent in the Brookhaven Protein Data Bank; T. Takano and R. E. Dickerson, *J. Mol. Biol.* **153**, 95 (1981).
16. It is difficult to develop a bridge Hamiltonian that is an exact translation of the Onuchic and Beratan "decay-per-bond" strategy. We use the definition in (*24*), where Onuchic and Beratan define [see table 1 in (*24*)] the site energy (diagonal matrix element) for all atoms in the molecule to be 0 (there is one orbital per site), the bonded atom hopping matrix element (β in Hückel theory) to be −0.881 eV, and the tunneling energy to be E = 2.0 eV; in the present work, we treat the tunneling energy as an adjustable parameter. To obtain the distance dependence of β for nonbonded atoms, we adapt an expression from (*5*)
$$\beta_{\text{nonbonded}}(r) = \lambda e^{-1\ 7(r-1\ 4)}$$
where r is the interatomic distance measured in angstroms. The prefactor λ is fixed by the requirement that $\beta(r_{CC}) = \beta_0/2$, where r_{CC} = 1.54 Å is the carbon-carbon bond length and β_0 = −0.881 eV is the bonded-atom hopping matrix element. Because the interaction between atoms separated by more than 8 Å is small, it is neglected.
17. Although Beratan and Onuchic write the effective coupling as an exponentially decreasing product, they find significant dependence on the chosen path. This may partially be a result of topological effects, but calculations that include all pathways between donor and acceptor indicate that single-pathway calculations overestimate fluctuations in the effective coupling at a given distance (*11*).
18. A. M. Brun, S. M. Hubig, M A. J. Rodgers, W. H. Wade, *J. Phys. Chem.* **96**, 710 (1992).
19. D. S. Wuttke, M. J. Bjerrum, J. R. Winkler, H. B. Gray, *Science* **256**, 1007 (1992).
20. M. A. Thompson and M. C. Zerner, *J. Am. Chem. Soc.* **113**, 8210 (1991).
21. H. Treutlein *et al.*, *Proc. Natl. Acad. Sci. U.S.A.* **89**, 75 (1992).
22. P. Siddharth and R. A. Marcus, *J. Phys. Chem.* **97**, 2400 (1993).
23. W. Feller, *An Introduction to Probability Theory and its Applications* (Wiley, New York, 1971).
24. J. N. Onuchic, P. C. P. de Andrade, D. N. Beratan, *J. Chem. Phys.* **95**, 1131 (1991).

25. This work was supported in part by a grant from the National Science Foundation. We thank M. D. Newton for comments on the manuscript.

4 June 1993; accepted 3 September 1993

Growth of High Aspect Ratio Nanometer-Scale Magnets with Chemical Vapor Deposition and Scanning Tunneling Microscopy

Andrew D. Kent,* Thomas M. Shaw, Stephan von Molnár, David D. Awschalom

A combination of chemical vapor deposition and scanning tunneling microscopy techniques have been used to produce nanometer-scale, iron-containing deposits with high aspect ratios from an iron pentacarbonyl precursor both on a substrate and on the tunneling tip itself. The structure and composition of the resulting nanodeposits were determined by transmission electron microscopy and high spatial resolution Auger electron spectroscopy. Either polycrystalline, relatively pure, body-centered-cubic iron or disordered carbon-rich material can be deposited, depending on the bias conditions of the tip sample junction and the precursor pressure. Two mechanisms of decomposition are inferred from the growth phenomenology.

The ability to control matter on decreasing length scales is expected to lead to significant scientific and technological advances. The scanning tunneling microscope (STM) offers the ultimate spatial resolution possible—manipulating materials down to the atomic level (*1*). For example, single atoms have been positioned on specific metal and semiconductor surfaces (*2–4*). The creation of interesting nanostructures requires the further ability to deposit a variety of different materials on substrates and to create clusters of atoms. Combining chemical vapor deposition (CVD) techniques with the STM offers great promise in this regard. Metal organic precursors are commercially available for many elements because of their widespread use in thin film technology (*5*). Furthermore, the local interactions present in an STM have already proved capable, in initial investigations (*6–10*), of decomposing certain precursors to leave behind metallic deposits. An additional and important challenge in such growth studies is knowing the nature of the resulting material. In general, it is difficult to characterize STM deposits by other microscopic or analytical techniques because of the small quantity of matter present (*11*). Although STM images provide an idea of the topology of small structures, it is not possible to discern their composition or crystalline phase.

We present here the results of an investigation of the growth of nanometer-scale iron deposits with a combination of CVD and STM techniques. In this study we were able to deduce the crystalline phase and composition of an STM deposit using transmission electron microscopy (TEM) and high-resolution Auger electron spectroscopy (AES). This leads to an understanding of the growth phenomenology and control of the resulting materials structure, composition, and shape on a nanometer scale. Specifically, we can control depositions on either the substrate or the tip by varying the growth conditions. We demonstrate the ability to produce high aspect ratio iron filaments with diameters less than 10 nm and aspect ratios greater than 80. Furthermore, by varying the bias conditions and precursor pressure we can form either amorphous or polycrystalline material. Filaments can be directly deposited on the apex of a silicon tip, which is part of a microfabricated silicon cantilever used in scanning force microscopy. Such nanodeposits will therefore find use in a variety of scanning probe microscopy experiments and are expected to extend the spatial resolution of these techniques.

We have used a modified commercial STM (*12*) in an ultrahigh vacuum (UHV) chamber (5×10^{-10} torr) designed to handle reactive gases over a wide range of

---

A. D. Kent, T. M. Shaw, S. von Molnár, IBM Research Division, T. J. Watson Research Center, Post office Box 218, Yorktown Heights, NY 10598.
D. D. Awschalom, Department of Physics, University of California, Santa Barbara, CA 93106.

---

*To whom correspondence should be addressed.

pressures (10^{-9} to 10^{-1} torr) (*13*). In most of our growth studies we have used iron pentacarbonyl [$Fe(CO)_5$] gas on silicon (111) substrates (*14*). This precursor has been used in thermal and photoassisted CVD of iron thin films (*5*) as well as in prior STM work (*10*). Moreover, transition metal carbonyls are known to decompose under low-energy electron bombardment, making them attractive candidates for STM deposition (*5*).

The precursor was introduced into the chamber, and the tip sample bias voltage was slowly raised at constant current until deposits formed on the substrate. Growth occurred in the field emission regime in which electrons have an energy greater than the work function of either the tip or the sample depending on the bias polarity. For $Fe(CO)_5$, we found that decomposition occurs at bias voltages as low as 5 V and that there is no minimum current down to 25 pA. However, the deposition was more reproducible at higher bias voltages (>15 V) and low current (~50 pA). During growth, the STM feedback loop retracts the tip to maintain a constant current, and thus constant height, between the tip and growing deposit. The tip was fully retracted when the deposit reached the desired height above the surface (*10*). After deposition the structures were imaged with the STM in the tunneling regime (bias, 2 V).

STM images of iron dots deposited on silicon are presented in Fig. 1. Figure 1A shows a single dot, 14 nm in diameter and 7 nm high, deposited at a tip bias of −25 V, a current of 50 pA, and a $Fe(CO)_5$ pressure of 10^{-6} torr. Visible in the background are monoatomic steps that run at a 25° angle from the *y* axis in this image. [The Si is miscut 1° from the (111) plane.] In a second experiment, we repeated the same deposition process in an array with 80-nm spacing (Fig. 1B). From these images, there is evidence for material deposited over an area of the surface around each dot. In Fig. 1B this background obscures the steps in the silicon surface. There is also a distribution of sizes evident in Fig. 1B with the smallest clusters having an approximate diameter of 10 nm. These are the smallest deposits we have been able to form with this precursor.

Considerable insight into the deposition process can be gained by forming larger dots. Scanning electron micrographs (SEMs) are shown in Fig. 2 of such deposits that are part of 100-dot arrays with 0.5-μm spacing. The dots were grown at a tip bias of −15 V and a current of 50 pA while the height and precursor pressure were varied between the different arrays. In Fig. 2A (pressure $P = 1 \times 10^{-5}$ torr) dots 35 nm in diameter and 70 nm high are shown. Material with a darker appearance in the SEM is found spread over a 300-nm diameter. The background consists of small ~10-nm particles. The result of growing 100-nm filaments ($P = 4 \times 10^{-5}$ torr) is shown in Fig. 2B. For these taller dots, secondary deposits fill the entire area between the elements in the array. Increasing the precursor pressure ($P = 4 \times 10^{-4}$ torr) while maintaining the same aspect ratio reduces the extent of the background deposits (Fig. 2C). The dot growth rate increases with pressure so that in Fig. 2C it is 100 nm/s. Thus, the time per deposit is reduced in Fig. 2C to 1 s relative to 10 s for the deposits in Fig. 2B. The corresponding reduction in the background is strong evidence for diffusion. For such a process the length r varies as $r \sim \sqrt{Dt}$, where D is the diffusion constant and t is the time. On the assumption that the diffusion constant is independent of pressure, a reduction in the deposition time by 10 s results in a factor of 3 decrease in the diffusion distance as approximately observed (compare Figs. 2B and 2C). We believe that the background of small clusters is due to a catalytic reaction of diffused reaction products with an absorbed precursor layer (*15*).

We used AES to determine the composition of the deposits depicted in Fig. 2. A depth profile revealed a contaminated carbon layer common to air- and SEM-exposed samples. After this layer (~12 nm) had been sputtered away, different areas were analyzed. Over a surface encompassing the entire matrix (5 μm by 5 μm) the composition of the arrays were similar [atomic percent: 42% iron, 52% carbon, and 6% oxygen (uncertainty of ±5%)]. An analysis with the electron beam focused on a dot from the array shown in Fig. 2A indicated

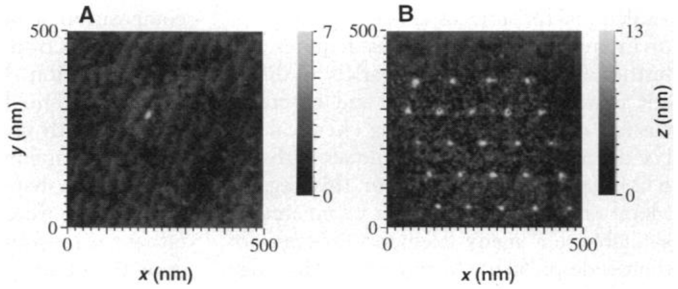

Fig. 1. STM images of iron dots formed at a tip bias of −25 V, a current of 50 pA, in a $Fe(CO)_5$ pressure of 10^{-6} torr. (**A**) Single dot; (**B**) a 5 × 5 element array, 80-nm spacing.

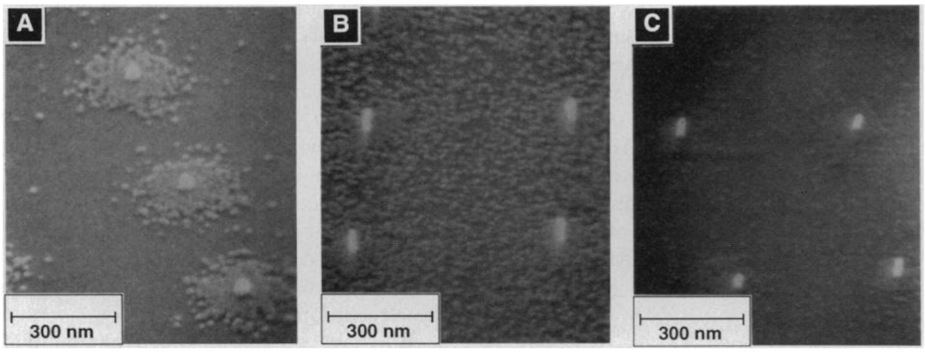

Fig. 2. Scanning electron micrographs (at a 45° tilt) of arrays deposited at a tip bias of −15 V, a current of 50 pA, and different pressures: (**A**) $P = 1 \times 10^{-5}$ torr; (**B**) higher aspect ratio deposits, $P = 4 \times 10^{-5}$; and (**C**) $P = 4 \times 10^{-4}$ torr.

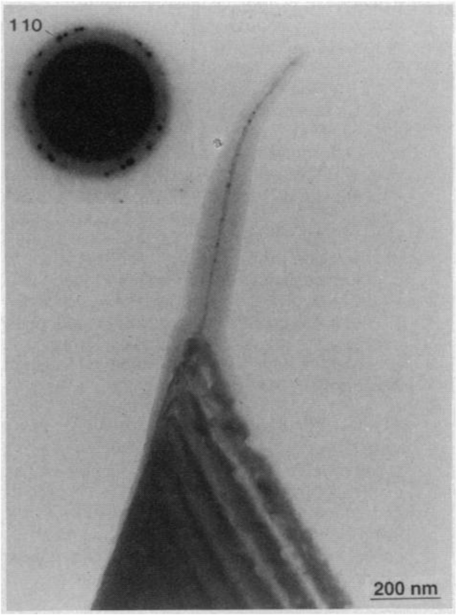

Fig. 3. Transmission electron micrograph of a high aspect ratio filament on the apex of a silicon tip. The inner filament shows diffraction contrast, has a diameter of 9 nm, and is 880 nm high. A ring of diffraction spots indexed to (110) planes of bcc iron is shown in the inset.

69% iron with the remainder being carbon, and oxygen below the detectable limit (1%). In Figs. 2B and 2C we found 63% and 50% iron, respectively. The area analyzed in these cases is limited by the electron beam and scattering to an area larger (~50 nm in diameter) than a single dot. Because the background has a higher carbon content, this analysis is likely to underestimate the metal content of the central deposits. The different geometry of the deposits complicates quantitative comparisons of the results among arrays. The decreasing iron signal reflects both the smaller dot diameter (~20 nm) in Figs. 2B and 2C and a reduction in the metal content with increasing precursor pressure. These qualitative results are consistent with TEM measurements (discussed below) that reveal a small central region of pure iron in a deposit.

Reversing the polarity of the voltage bias, electrons are field-emitted from the sample and similar dots can be deposited on the STM tip. Structural analysis can then be performed with TEM. An image of an 880-nm-long filament on a microfabricated silicon tip is shown in Fig. 3 ($P = 7 \times 10^{-5}$ torr; tip bias, +15 V; and current, 50 pA). A contamination coating around a denser interior is observed in the micrograph. This layer is built up during prior SEM and TEM observation of this structure. The internal core shows diffraction contrast indicative of a polycrystalline material with the grain size approximately equal to the fiber diameter (~9 nm). In diffraction, six distinct lines were visible, each of which could be indexed to the body-centered-cubic (bcc) phase of iron. The most intense ring of (110) spots is indicated in the inset of Fig. 3. This phase is a ferromagnet at room temperature. At carbon concentrations >0.4%, however, the equilibrium phase of Fe–C is face-centered-cubic. The presence of the bcc phase is evidence for pure iron and nearly complete decompositon of the precursor. We repeated the TEM measurements 2 months after growth and found no change in either the central fiber diameter or the diffraction pattern. The deposit with the contamination coating is thus stable against oxidation in air.

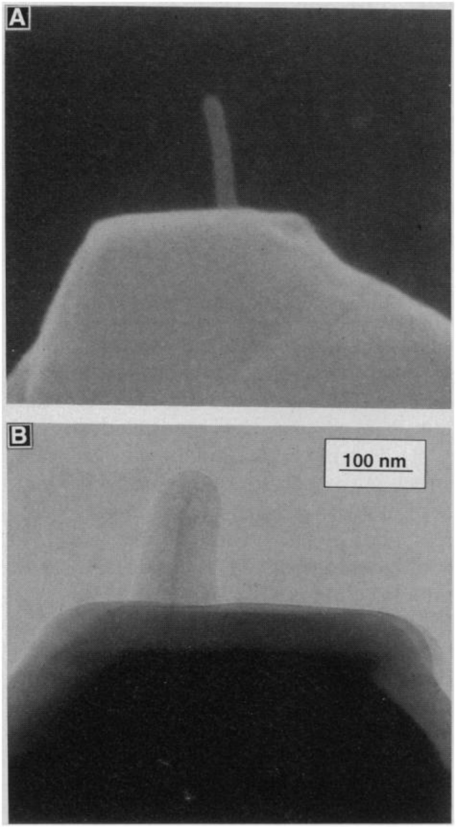

Fig. 4. (**A**) SEM and (**B**) TEM micrographs at the same magnification of a filament grown on a negatively biased silicon tip. The as-deposited filament had a diameter of 7 nm and a height of 150 nm.

Susceptibility measurements of arrays of dots (20 nm in diameter by 50 nm high with 1-μm spacing) deposited in the input coil of a superconducting quantum inference device (SQUID) indicate that these dots are indeed magnetic. The susceptibility increases with decreasing temperature, indicative of paramagnetic behavior, and saturates at low temperature (150 mK). The magnitude of the signal corresponds to 3.7×10^5 spins per particle and is consistent with the expected number of iron atoms in each dot (*16*).

Growth also occurs on the negatively biased surface. For example, during the formation of arrays on a positively biased substrate (as in Fig. 2), filaments also grow on the tip. Inspection of a tip in an SEM reveals the formation of a nanofilament on its apex (Fig. 4A). This structure was grown on a silicon tip at a bias of -15 V while 25 100-nm tall dots were formed on a substrate ($P = 6 \times 10^{-5}$ torr). The growth rate of 8 nm/s is 1/16 of that on the opposing sample. The resulting structure is conducting and stable enough to be used to image the surface of silicon in the tunneling regime (bias, 2 V).

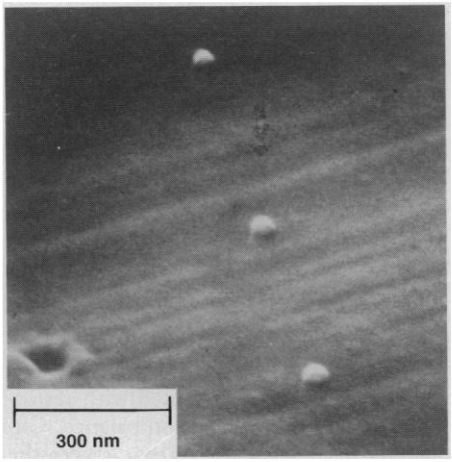

Fig. 5. Dots (40 nm in diameter) deposited in rough areas of a negatively biased (-15 V) substrate. Under these conditions deposits are not formed in adjacent smooth regions of the substrate.

In a TEM micrograph of the same tip (Fig. 4B) we again observe a layer over a denser core. Because of contamination buildup, the overall diameter of the fiber has appeared to increase between the SEM and TEM observations. The as-deposited filament had a diameter of 7 nm and was 150 nm in length. Unlike the case in Fig. 3, there is no diffraction contrast in the micrograph, nor were we able to record a diffraction pattern. This result implies that the material is amorphous or that the grain size is significantly less than the fiber diameter.

A high local electric field appears to be necessary to form such structures. The local surface topology thus influences their placement and growth. For example, on a negatively biased substrate, we find little or no growth in flat regions. However, in rough areas in which larger local fields are generated, deposits form. This is shown in Fig. 5, where we have produced a sequence of dots in a part of the substrate that has been scribed with a diamond tip. There are no secondary deposits in this case. An AES analysis reveals an approximate composition of 10% iron and 90% carbon, with oxygen below the detectable limit. This carbon-rich material is very different from the material produced on a positively biased substrate, where the iron content determined by AES was always greater than 50% and the detailed TEM analysis showed pure iron.

We associate different mechanisms of decomposition of the precursor with the two distinct growth modes we have observed. Energetic electrons are primarily responsible for the deposition on the positively biased surface. Electron impact dissociation probably dominates in this case as in plasma and electron beam deposition (*5*). On the negative surface, a field-induced reaction occurs. Such a mechanism has been used to produce whiskers and dendrites on emitter tips from tungsten hexacarbonyl, $W(CO)_6$, (*17*). The strong local fields in an STM are expected to influence the decomposition to a certain degree on both surfaces. For example, the extreme polarizability of $Fe(CO)_5$ (*18*) may be important in drawing molecules into the high local field region under the tip.

The growth phenomenology, however, is very different for these two modes (electron- or field-induced decomposition). For electron-induced growth, although the decomposition occurs locally, the reaction products are mobile on the surface. Here we believe an analogy can be drawn between the deposition of nanoscale filaments and thin film nucleation and growth theory. We observe that metallic ($>50\%$ iron) deposits do not grow until the decomposition rate is sufficiently rapid that critically sized clusters form under the tip. This rate, in the present experiments, is limited by the adsorption of precursors on the surface and hence the pressure. We find that below $\sim 10^{-6}$ torr filaments do not form and the reaction products are dispersed on the surface like the background in Fig. 2. As we have illustrated, increasing the pressure reduces the spatial extent of the background and allows the formation of iron-rich deposits. The minimum diameter of metallic clusters is ~ 10 nm. We expect that smaller iron clusters could be formed if the mobility of adatoms on the surface were reduced by, for example, cooling the substrate.

In contrast to this behavior, in the case of field-induced reactions, there is little or no diffusion of material. The reaction occurs in the high-field regions of the STM junction, and the products are apparently immobilized. The resulting structures are carbonaceous filaments with a small percentage of iron.

In conclusion, the ability to fabricate and position magnets on a nanometer scale offers unique scientific and technological opportunities. For example, increasing the storage capacity of magnetic media requires, among other important practical considerations, reducing the size of magnetized domains. At a certain dimension even in the absence of thermal activation, macroscopic quantum tunneling of the magnetization is predicted to occur and to present a fundamental quantum limit to magnetic storage (*19*). Moreover, the combination of nanomagnets with present semiconductor technology may lead to new classes of magnetically active devices that rely on the interplay between magnetic and electronic degrees of freedom in confined geometries. STM structures will permit studies of the ramifications of such magnetic miniaturization.

REFERENCES AND NOTES

1. For a recent review, see, for example, C. F. Quate, in *Highlights of the 80's and Prospects for the 90's in Condensed Matter Physics*, L. Esaki, Ed. (Plenum, New York, 1991), pp. 573–630.
2. D. M. Eigler and E. K. Schweizer, *Nature* **344**, 524 (1990).
3. L. J. Whitman, J. A. Stroscio, R. A. Dragoset, R. J. Celotta, *Science* **251**, 1206 (1991).
4. I.-W. Lyo and P. Avouris, *ibid.* **253**, 173 (1991).
5. For a recent review, see P. A. Dowben, J. T. Spencer, G. T. Stauf, *Mater. Sci. Eng. B* **2**, 297 (1989).
6. R. M. Silver, E. E. Ehrichs, A. L. de Lozanne, *Appl. Phys. Lett.* **51**, 247 (1987).
7. E. E. Ehrichs, R. M. Silver, A. L. de Lozanne, *J. Vac. Sci. Technol. A* **6**, 540 (1988).
8. E. E. Ehrichs, W. F. Smith, A. L. de Lozanne, *Ultramicroscopy* **42–44B**, 1438 (1991).
9. M. A. McCord, D. P. Kern, T. H. P. Chang, *J. Vac. Sci. Technol. B* **6**, 1877 (1988).
10. M. A. McCord and D. D. Awschalom, *Appl. Phys. Lett.* **57**, 2153 (1990).
11. Somewhat larger scale deposits produced by high-voltage electron beam decomposition of metal organics have been characterized by TEM and AES. See, for example, K. L. Lee and M. Hatzakis [*J. Vac. Sci. Technol. B* **7**, 1941 (1989)] and S. Matsui and T. Ichihashi [*Appl. Phys. Lett.* **53**, 843 (1988)].
12. Burleigh Instruments–ARIS 5100 UHV-STM.
13. An optical microscope provides a view of the tip-sample junction, and a coarse *x-y* sample translation stage allows positioning of the tip with respect to registration marks on the substrate. Positional control is necessary for locating deposits for analysis in an SEM and AES system.
14. The wafers were chemically cleaned and hydrogen terminated by dipping in dilute HF (5:1 H_2O:HF) just before being put in vacuum. They were then flashed (5 to 10 s) in situ to 700°C to desorb the hydrogen and leave a clean silicon surface. The depositions were performed at room temperature with both electrochemically etched tungsten wire and microfabricated silicon tips (Nanoprobe, Aidlingen, Germany, noncontact atomic force microscopy all-silicon integrated cantilevers).
15. Iron pentacarbonyl is autocatalytic, decomposing in the presence of iron. See, for example, (*18*).
16. D. D. Awschalom, A. D. Kent, S. von Molnár, in preparation.
17. H. B. Linden, E. Hilt, H. D. Beckey, *J. Phys. E* **11**, 1033 (1978).
18. D. F. Shriver and K. H. Whitmore, in *Comprehensive Organometallic Chemistry*, G. Wilkinson, F. Stone, E. Abel, Eds. (Pergamon, New York, 1982), vol. 4, pp. 243–319.
19. D. D. Awschalom, D. P. DiVincenzo, J. F. Smyth, *Science* **258**, 414 (1992).

20. We thank D. Beach, M. McCord, M. Yu, and D. DiVincenzo for helpful advice and discussions and B. Schad for the AES measurements. This work was supported in part by the Air Force Office of Scientific Research grant F49620-93-1-0117.

9 July 1993; accepted 8 September 1993

Uncertainties in Carbon Dioxide Radiative Forcing in Atmospheric General Circulation Models

R. D. Cess, M.-H. Zhang, G. L. Potter, H. W. Barker,
R. A. Colman, D. A. Dazlich, A. D. Del Genio, M. Esch,
J. R. Fraser, V. Galin, W. L. Gates, J. J. Hack, W. J. Ingram,
J. T. Kiehl, A. A. Lacis, H. Le Treut, Z.-X. Li, X.-Z. Liang,
J.-F. Mahfouf, B. J. McAvaney, V. P. Meleshko, J.-J. Morcrette,
D. A. Randall, E. Roeckner, J.-F. Royer, A. P. Sokolov,
P. V. Sporyshev, K. E. Taylor, W.-C. Wang, R. T. Wetherald

Global warming, caused by an increase in the concentrations of greenhouse gases, is the direct result of greenhouse gas–induced radiative forcing. When a doubling of atmospheric carbon dioxide is considered, this forcing differed substantially among 15 atmospheric general circulation models. Although there are several potential causes, the largest contributor was the carbon dioxide radiation parameterizations of the models.

The most comprehensive way to estimate climate change caused by increasing concentrations of greenhouse gases is to use three-dimensional general circulation models (GCMs). But even for the most straightforward climate-change simulation, a change in equilibrium climate that results from a doubling of atmospheric CO_2, there is a roughly threefold variation in the predicted increase in global mean surface temperature (*1*, *2*) (Fig. 1). Global climate change caused by a CO_2 doubling may be conceptually interpreted as a two-stage process: forcing and response. The forcing is the direct radiative perturbation caused by the CO_2 increase, whereas the response is the climate change associated with restoring the global-mean radiation balance. Climate feedback mechanisms that govern the response differ substantially among GCMs (*3–7*), but it is not known to what extent differences in Fig. 1 are attributable to variations in forcing among models. In an earlier comparison (*8*), significant differences were found in CO_2 radiative forcing from radiation codes used in several GCMs.

Potential forcing differences attributable to other facets of the GCMs were not, however, addressed. These included:

1) Forcing is dependent on lapse rate, which is the decrease of atmospheric temperature with height. Because CO_2 forcing is a change in the greenhouse effect, it could be affected by differences in lapse rate among models (*9*).

2) The forcing is substantially reduced through radiative overlap of the CO_2 absorption bands by the absorption of water vapor (*8*), so differences in atmospheric water vapor distributions among models could likewise affect CO_2 forcing, as well as differences in the parameterization of radiative overlap in the radiation codes.

3) Clouds also reduce the forcing (*10*), so the substantial differences among different GCMs' cloud fields (*6*) could cause forcing differences.

In this study we specifically address these